A framework for simultaneous optimization of topology and filter configurations through local density interpolation

Giele, Reinier; Ayas, Can; Langelaar, Matthijs

DOI
10.1080/0305215X.2025.2568914

Publication date
2025

Document Version
Final published version

Published in
Engineering Optimization

Taylor & Francis
Taylor & Francis Group

Engineering Optimization

ISSN: 0305-215X (Print) 1029-0273 (Online) Journal homepage: www.tandfonline.com/journals/geno20

A framework for simultaneous optimization of topology and filter configurations through local density interpolation

Reinier Giele, Can Ayas & Matthijs Langelaar

To cite this article: Reinier Giele, Can Ayas & Matthijs Langelaar (17 Oct 2025): A framework for simultaneous optimization of topology and filter configurations through local density interpolation, Engineering Optimization, DOI: 10.1080/0305215X.2025.2568914

To link to this article: https://doi.org/10.1080/0305215X.2025.2568914

Published online: 17 Oct 2025.

ENGINEERING OPTIMIZATION
https://doi.org/10.1080/0305215X.2025.2568914

Taylor & Francis
Taylor & Francis Group

OPEN ACCESS Check for updates

A framework for simultaneous optimization of topology and filter configurations through local density interpolation

Reinier Giele, Can Ayas and Matthijs Langelaar

Faculty of Mechanical Engineering, Delft University of Technology, Delft, The Netherlands

ABSTRACT

A framework is proposed for geometric filters in density-based topology optimization. Most geometric filters feature density detection in a specified region of interest. In this method, this operation is decoupled from the finite element mesh by using interpolated densities. This allows for the filter configuration (*e.g.* tool orientation or printing direction) to be optimized simultaneously with the geometric layout. The framework is presented in a generic manner, and demonstrated on filters for: milling with simultaneous optimization of milling orientation; jetting with simultaneous optimization of jetting positions; and printing with simultaneous optimization of printing orientation. The performance of the framework is tested with numerical examples for compliance in 2D and 3D on a structured mesh, and in 2D on an unstructured mesh. The framework can extend the design freedom of existing filters, and can serve as a basis for the development of new geometric filters.

ARTICLE HISTORY
Received 4 February 2025
Accepted 26 September 2025

KEYWORDS
Topology optimization; geometry; accessibility; additive manufacturing; milling

1. Introduction

Topology Optimization (TO) is a computational design method that enables superior designs. One key aspect of its success is that only a few inputs are required to generate an optimized geometric layout of a component. In order to make TO more widely applicable for industrially relevant problems, various design requirements have to be accounted for such as manufacturability. Methods have been developed to ensure specific geometric conditions. Several methods ensure a manufacturable design, for example for additive manufacturing (Gaynor and Guest 2016; Langelaar 2016), milling (Høghøj and Träff 2022; Langelaar 2019; Mirzendehdel, Behandish, and Nelaturi 2020), moulding (Gersborg and Andreasen 2011; Yoon and Ha 2021) and general manufacturability (Chen, Lu, and Wei 2016). Moreover, methods have been developed to ensure a component's surface access during usage, for example cleanability (Giele, Ayas, and Langelaar 2024; Giele, van Keulen, and Langelaar 2022).

Geometric constraints are usually imposed through a filter that converts an input density field into, for instance, a manufacturable field. Filtering ensures full compliance with the desired geometric requirement in every design iteration. Note that the availability of such a strict filter also allows for reformulations using either hard or soft constraints, by quantifying the difference between the input and filtered fields–see for example van de Ven, Ayas, *et al.* (2018). Hence, a filter provides both rigour and versatility, and therefore in this article the focus is on various filter implementations within TO. This is done in the context of density-based TO.

CONTACT Reinier Giele r.j.p.giele@tudelft.nl

Geometric filters often involve settings that are chosen a priori by the designer, *e.g.* the milling tool orientation or printing direction. These predefined settings are referred to as *filter configuration settings*. Conventionally in the majority of filtering schemes, these are defined and remain fixed. However, for design problems that allow some flexibility, fixing the filter configuration limits the design freedom severely and unnecessarily. Allowing for the filter configuration to change as a part of the optimization process is therefore desired.

One example of this idea is to co-optimize the milling direction in a milling process, when only a single direction is allowed. Another example is seen in constraints for additive manufacturing, where the printing orientation could be co-optimized with the design. Several case-specific methods exist for simultaneous optimization of the geometric filter direction/orientation during the topology optimization. For example, for additive manufacturing, the influence of the printing orientation in the context of overhang filters has been addressed by, for example, Langelaar (2018). Simultaneous structural optimization and printing orientation has been addressed, for example, by Olsen and Kim (2020), Wang and Qian (2020) and Wang (2022). Simultaneous topology and milling orientation optimization for multiaxis machining has been presented by Gasick and Qian (2021). While all these examples have shown degrees of effectiveness, they are specific solutions for one geometric constraint case. A generic approach thus far is missing.

A second shortcoming of many existing geometric filters is that the filter operation is mesh dependent. The gathering of density information for existing filters is often performed with input from a single element or information defined at element centroids on a discretized grid. This can cause mesh dependency, which is, for example, demonstrated in the work of Delissen *et al.* (2022). Also, it is not always clear how geometric filters defined on a structured grid can be extended to unstructured grids, widely used in industrial applications. Mesh independent overhang filtering is, for example, proposed by Gaynor and Guest (2016), where an unstructured mesh is mapped on points, and by van de Ven, Ayas, *et al.* (2018), where a front propagation method is used to detect unprintable regions. Again, these are case-specific solutions that do not carry over to new use cases in a straightforward manner.

To address these challenges in this article, a general framework is presented that allows for co-optimization of the filter configuration for a wide variety of geometric filters and arbitrary meshes. Although different geometric filters serve different purposes, there are several important commonalities. These commonalities allow different geometric filters to be approached similarly within a general framework. Consequently, the proposed methodology in principle can be relevant for all geometric filters used in TO. This eliminates the need for case-specific solutions and facilitates the implementation of new filters.

In the presented framework, the filter configuration settings become additional design variables termed *filter configuration design variables*. This is done by considering neighbouring elements during the filtering process. In the filter definition, regions of interest are approximated with input and output points, which are decoupled from the computational domain discretization. Through local filtering operations, element quantities are linked to these decoupled points. As a result, a smooth variation of regions of interest is possible. Consequently, the filter configuration design variables related to the region of interest (*e.g.* milling tool orientation, jet source location, print orientation) can be changed and optimized, with consistent sensitivities for these new design variables. This allows for simultaneous gradient-based optimization of the design and the filter configuration design variables, resulting in an increase in design freedom.

In Section 2, the general framework is explained in detail. Throughout the article, the general framework is demonstrated on three example filters: milling, jetting and printing, for which the specific implementation is given in Section 3. Numerical examples are shown in 2D and 3D in Section 4. This is followed by a discussion and conclusions in Sections 5 and 6, respectively. An example for how the sensitivities can be calculated is given in Appendix 1. A comparison with existing methods is given in Appendix 2.

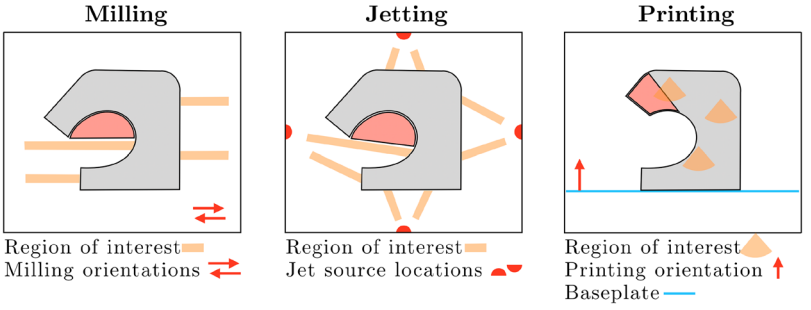

Figure 1. Schematic illustration of three different geometric filters. The original design is light grey, impermissible regions are marked in red/black. The three filters are detailed in Section 3. For all filters, the regions of interest (marked in orange/grey) are dependent on the *filter configuration settings* (the milling orientations, the jet source locations and the printing orientation).

2. Framework

Recall that the proposed method is intended for density-based TO. The filter turns an input density field $\mathbf{x}$ into a filtered output density field $\hat{\mathbf{x}}$, for which certain geometric requirements are satisfied. For simplicity, the framework is presented considering a 2D structured finite element mesh; however, extensions to an unstructured grid and to 3D follow naturally. Section 2.1 describes the commonalities between seemingly different geometric filters. Next, the general concept and nomenclature are explained in Section 2.2, and the general equations from $\mathbf{x}$ to $\hat{\mathbf{x}}$ are given in Section 2.3.

2.1. Commonalities between geometric filters

Although different geometric filters serve different purposes, there are several commonalities. In order to help understand the commonalities, three specific filters are first illustrated schematically in Figure 1. The details of each filter are described extensively in Section 3. It can be seen that, for each specific filter, a region of interest is inspected to see if the design adheres to the geometric constraints, or if there is any solid material in the impermissible region.

Now the commonalities of a geometric filter are shown more generally in Figure 2. First, since the topology of the structure is unknown in advance, the desired geometric requirement should be analysed in the entire domain. Therefore, the entire design domain is covered with a finite number of *checkpoints*, where a certain geometric requirement should be met. Whether the geometric requirement is met at a checkpoint is determined through gathering density information within a region of interest, the *detection region*, associated with the checkpoint of interest. This region can be at a single element, a line, or an area connected to the checkpoint. The detection region may also have a specific orientation, size and/or position, here referred to as the *detection region configuration*, which depends on the specific filter configuration setting—for example the milling tool orientation for machinability, the jet source location for jettability, or the printing orientation for additive manufacturability.

Secondly, by feeding the gathered density information to a *filter function* at every checkpoint, output densities are calculated. The output density should be such that the geometric requirement is met at the checkpoint. The filter function should also be differentiable to be suitable for gradient based optimization, and for smooth convergence it is desirable to add as little nonlinearity as possible to the optimization problem.

Thirdly, the output is created by projecting calculated output values at output points onto an output field. Usually, output points are at the checkpoints, but other cases will also be shown where output points do not coincide with the checkpoint.

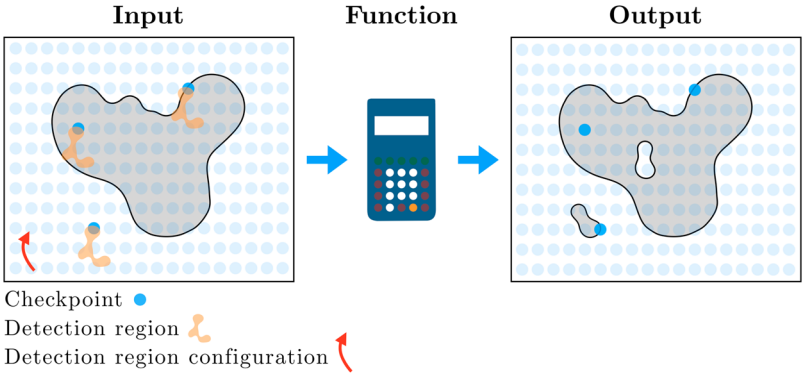

Figure 2. Schematic illustration of the general geometric filter concept, with three checkpoints highlighted. Density detection is performed on the input density field, based on which an output field is created. The *detection region configuration* is based on the *filter configuration setting* (shown with red/black arrow), *e.g.* the mill orientation, the jet location, or the printing orientation. On the right, a filtered output design is shown.

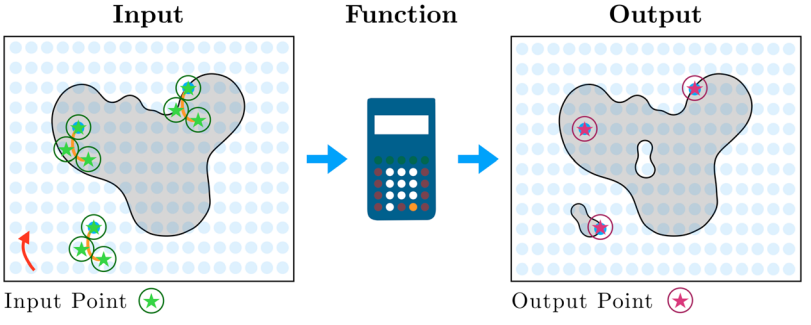

Figure 3. Schematic illustration of a generic geometric filter, with three checkpoints highlighted. The density detection (left) is performed at input points with (interpolated) input densities. The output field (right) is created at output points with the associated output densities.

2.2. General concept and nomenclature

The first step is the application of the well-known convolution filter $\mathcal{D}$ with radius R, which turns the density design variables $\mathbf{x}$ into $\tilde{\mathbf{x}}$, where $\tilde{\mathbf{x}} = \mathcal{D}(\mathbf{x})$ (Bourdin 2001; Bruns and Tortorelli 2001). This step is not explained further here, since it is widely used in density-based TO.

Next, in the proposed method the density detection is done with selected Input Points (IPs), which form a discretized representation of the detection region, depicted in Figure 3 (left). Next, at each IP, an *input density*, is computed from the $\tilde{\mathbf{x}}$ field. In existing filters, single element density values are sometimes used to represent the density state in the detection region but, to decouple the density detection in the detection region from the finite element mesh here, it is proposed to use interpolated densities at IPs. Subsequently, by performing the filter specific filter function on the input densities, an *output density* is computed. At the Output Point (OP), this output density value is projected onto a field such that a design is created which fulfils the filter requirements (depicted in Figure 3, right).

An overview of the steps and symbols used is given in Figure 4. The filter configuration design variables are referred to as α. For the milling filter, the new design variable α_m describes the milling orientation; for the jetting filter, the new design variable α_j describes the jet location; and for the printing filter, the new design variable α_p describes the printing orientation.

The coordinates of an IP are denoted by $\mathbf{c}^{(\mathrm{IP})}$, where the location is computed with a filter specific function $\mathbf{c}^{(\mathrm{IP})} = \mathcal{H}(\alpha)$. The input density is denoted by $\chi^{(\mathrm{IP})}$. Subsequently, by performing the filter

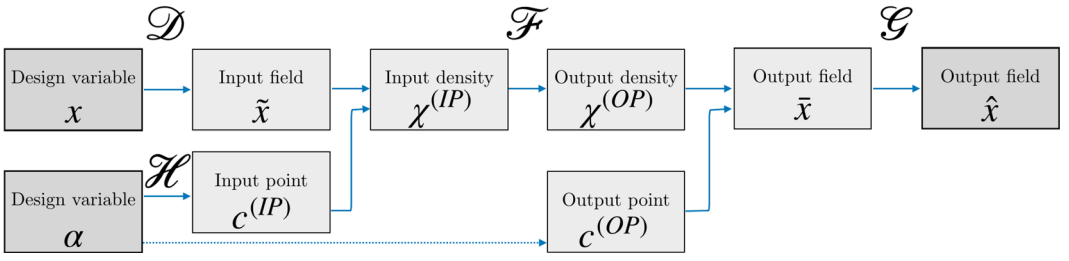

Figure 4. Overview of the steps of the geometric filtering framework. The dependency of the output point on design variable α is optional, depending on the specific filter. The operations $\mathcal{F}$, $\mathcal{G}$ and $\mathcal{H}$ are specific for each geometric filter.

specific filter function $\mathcal{F}$ on the input densities, an *output density*, $\chi^{(\mathrm{OP})}$, is computed, *i.e.* $\chi^{(\mathrm{OP})} = \mathcal{F}(\chi^{(\mathrm{IP})})$. At the OP, this output density value is projected onto a field to obtain $\bar{\mathbf{x}}$. Finally, some post filter functions of general form $\hat{\mathbf{x}} = \mathcal{G}(\bar{\mathbf{x}})$ can be applied to obtain the final output field $\hat{\mathbf{x}}$.

Finally, throughout the article, $\square^{(\mathrm{IP})}$ and $\square^{(\mathrm{OP})}$ are used as labels for symbols related to the filters, and not as indices. Similarly, the labels $\square^{(\mathrm{m})}$, $\square^{(\mathrm{j})}$ and $\square^{(\mathrm{p})}$ are used to refer to milling, jetting and printing, respectively. For the α design variable, this label is left out. Indexes are written in italic and subscript, as is conventional. The comma in the subscript does not denote differentiation, but is used for multiple indexes.

2.3. General input–output relations

The IPs are used for density detection in the detection region. The detection region is defined according to the specific geometric filter requirements. For example for milling, this is the region between the checkpoint and the location where the tool enters the domain. For jetting, this is the region between the checkpoint and the jet source location. For printing, this is the region immediately below the checkpoint according to the printing orientation, considering an overhang angle. The computation for the detection region, thus the IPs, is explained in the filter specific sections.

The input density is the weighted average of the densities within a circular interpolation domain of radius $R^{(\mathrm{IP})}$. The input density is calculated with a convolution filter centred at the IP using the smoothened density values of the underlying mesh, as visualized in Figure 5. The weights of the element densities depend on the distance between the element centre and the IP. This allows for smooth changes in the detection region configuration and hence calculation of the sensitivities.

$$w_e^{(\mathrm{IP})}(\mathbf{c}^{(\mathrm{IP})}) = \max(0, R^{(\mathrm{IP})} - \|\mathbf{c}_e - \mathbf{c}^{(\mathrm{IP})}\|), \tag{1}$$

where $w_e^{(\mathrm{IP})}$ is the linear weight function between the IP and element e. $\mathbf{c}^{(\mathrm{IP})}$ and $\mathbf{c}_e$ are the coordinates of the IP and the centroid of element e, respectively. Next, the weights $w_e^{(\mathrm{IP})}$ are normalized such that their values range between zero and one, and all weights related to e sum to one:

$$\check{w}_e^{(\mathrm{IP})}(\mathbf{c}^{(\mathrm{IP})}) = \frac{w_e^{(\mathrm{IP})}}{\sum_{j=1}^{N_{\mathrm{el}}} w_j^{(\mathrm{IP})}}, \tag{2}$$

where N_{el} is the total number of elements in the domain. It remains to calculate $\chi^{(\mathrm{IP})}$ from the smoothed density field $\tilde{\mathbf{x}}$ using the normalized weights $\check{w}_e^{(\mathrm{IP})}$:

$$\chi^{(\mathrm{IP})}\left(\tilde{\mathbf{x}}, \mathbf{c}^{(\mathrm{IP})}\right) = \sum_{e=1}^{N_{\mathrm{el}}} \tilde{x}_e \check{w}_e^{(\mathrm{IP})}. \tag{3}$$

Finally, it is important to emphasize that $\chi^{(\mathrm{IP})}$ depends not only on the density design variables, but also on the IP location $\mathbf{c}^{(\mathrm{IP})}$, and thus on the new filter configuration design variable α, such that the

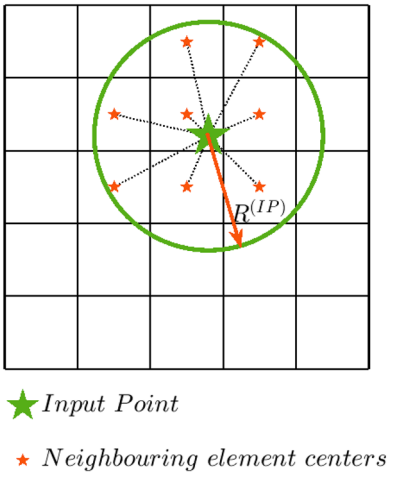

Figure 5. An Input Point (IP) is the location where the input density is calculated. It is computed as the weighted average of smoothed densities $\tilde{x}_e$ from the elements with centres in the interpolation domain.

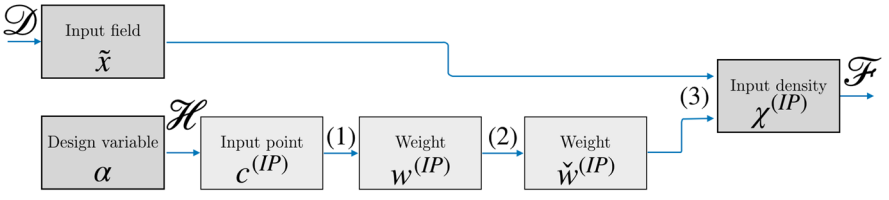

Figure 6. The flow diagram illustrating calculation of input density $\chi^{(\mathrm{IP})}$ from a density field $\tilde{\mathbf{x}}$ and the filter configuration design variable α. The numbers in parentheses represent the equations used for each step. By following the steps in reverse order, calculating derivatives, and through the chain rule, the sensitivities are calculated.

sensitivities with respect to the detection region configuration can be calculated. Figure 6 illustrates how the sensitivities of the input density with respect to $\tilde{\mathbf{x}}$ and α can be calculated. The steps from left to right correspond to Equations (1)–(3). Following the steps in reverse order, taking the derivatives, and using the chain rule leads to the sensitivities for the $\tilde{x}$ and α design variables.

Once the input densities have been calculated, it remains to perform the filter function, based on the specific filter characteristics, yielding the output value $\chi^{(\mathrm{OP})}$. This operation should ensure that the filter requirements are met on the checkpoint. This very much depends on the specific filter and is therefore discussed further in the following filter specific sections (Sections 3.1–3.3). The filter operation should also be smooth so that the sensitivities can be calculated consistently.

Lastly, the output field $\bar{\mathbf{x}}$ is created, which is often a density field. First, at each OP, an output value $\chi^{(\mathrm{OP})}$ is projected onto one or more elements in its close proximity onto the field $\check{\mathbf{x}}$. Often, the OP coincides with the checkpoint; however, examples with different locations will be shown in this article. The projection is also carried out with a convolution filter, for which the weights on elements e are first calculated:

$$w_e^{(\mathrm{OP})}(\mathbf{c}^{(\mathrm{OP})}) = \max\left(0, R^{(\mathrm{OP})} - \|\mathbf{c}^{(\mathrm{OP})} - \mathbf{c}_e\|\right), \tag{4}$$

where $R^{(\mathrm{OP})}$ is the output convolution filter radius, and $\mathbf{c}^{(\mathrm{OP})}$ and $\mathbf{c}_e$ are the coordinates of the OP and the centroid of element e, respectively. Again, the weights are normalized:

$$\check{w}_e^{(\mathrm{OP})}(\mathbf{c}^{(\mathrm{OP})}) = \frac{w_e^{(\mathrm{OP})}}{\sum_{j=1}^{N_{\mathrm{el}}} w_j^{(\mathrm{OP})}}. \tag{5}$$

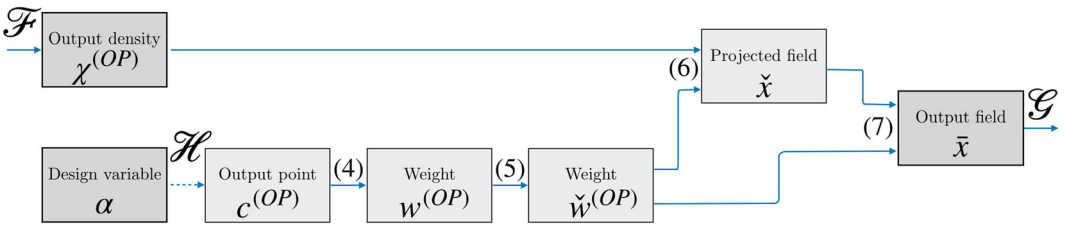

Figure 7. The flow from the output density (and potentially the filter configuration design variable α), to the output field. The numbers in parentheses represent the equations used for each step. By following the steps in reverse order, and through the chain rule, the sensitivities follow naturally.

The output density value is projected onto field $\check{\mathbf{x}}$ as follows:

$$\check{x}_e = \chi^{(\mathrm{OP})} \check{w}_e^{(\mathrm{OP})}. \tag{6}$$

To account for elements getting multiple contributions from multiple OPs, the final output value for element e is obtained by dividing by the sum of the contributions:

$$\bar{x}_e(\tilde{\mathbf{x}}) = \frac{\sum_{i=1}^{n_e} \check{x}_{e,i}}{\sum_{i=1}^{n_e} \check{w}_{e,i}^{(\mathrm{OP})}}, \tag{7}$$

where n_e is the number of contributions on element e, and $\check{x}_{e,i}^{(\mathrm{OP})}$ and $\check{w}_{e,i}^{(\mathrm{OP})}$ are the value and weight of the individual contributions of different input points i. Finally, it should be mentioned that, in many cases, $R^{(\mathrm{OP})}$ is small so that the output value is projected to a single element only. The dependency of the output field $\bar{\mathbf{x}}$ on the output density (and potentially α) is illustrated in Figure 7.

3. Examples of geometric filters

In this section, the framework is applied to milling, jetting and printing filters, respectively. The basic concepts of these filters and the ways filter configuration design variables can enhance design freedom are illustrated in Figure 8. In milling, the component's surface should be reachable by the milling tool, with orientations that can be optimized as well. For jetting, the component's surface should be reachable by the jetted fluid, originating from jet source locations that are to be optimized. Thirdly, for printing, material can only be built upon previously deposited material (or the baseplate) considering a critical overhang angle and according to a printing orientation, which can also be optimized simultaneously. The three filters and their implementation in the proposed framework are introduced below.

3.1. Milling with tool orientation optimization

In this section, the first example is given of how the general framework can be applied to a milling filter with an adjustable tool orientation, inspired by Langelaar (2019), but now with simultaneous optimization of milling tool orientation. The milling filter ensures that a component can be manufactured with 2.5D milling, such that tools should have access to the entire component surface. Thus undercuts or internal holes are not admissible. Consequently, tool path access is considered while neglecting the tool size for simplicity. In density-based TO, this means that regions further downstream of the tool path should not have a lower density than regions encountered upstream. The tool access orientations are traditionally defined a priori and remain constant throughout the optimization. However, in this new filtering framework, the milling orientation is the filter configuration design variable designated as α_m. In the explanation in the first part of this section, only one milling orientation is considered.

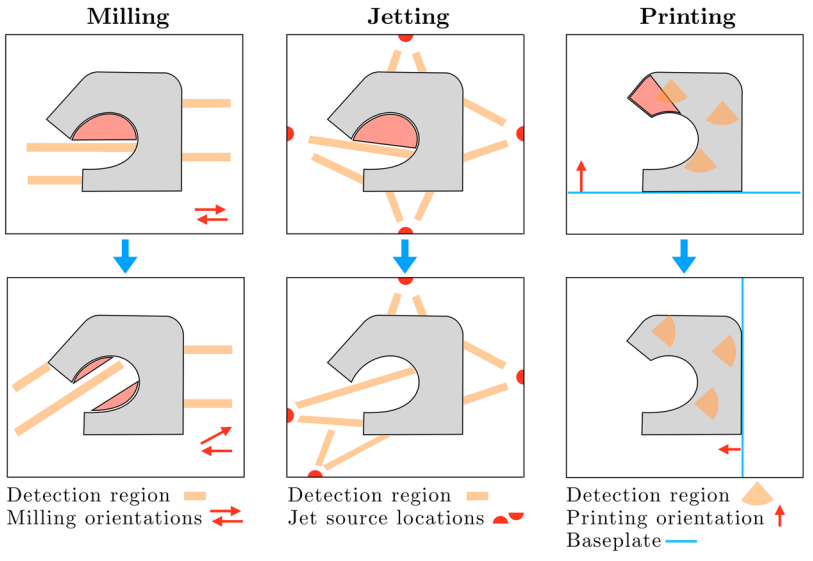

Figure 8. The influence of the *filter configuration design variables* on the design freedom for three example filters. The original design is light grey, forbidden regions are marked in red/black. The three filters are discussed in Section 3. Top: designs with random filter configuration settings. Bottom: design with more favourable filter configuration settings.

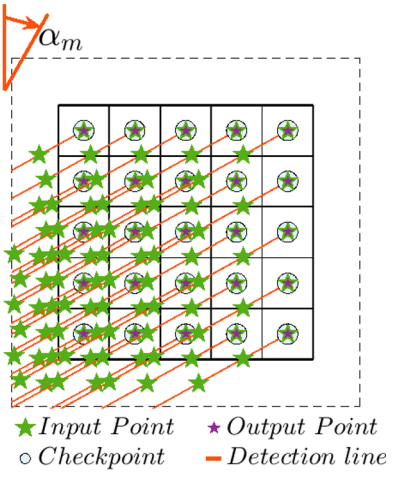

Figure 9. Schematic illustration of a milling access filter. The checkpoints are located in all elements.

According to the general framework, the checkpoints should be located at all element centres within the domain. The detection region for each checkpoint becomes the region around a straight line upstream in the milling orientation. This is shown in Figure 9.

However, for computational gains, it is possible to reduce the number of checkpoints, since many detection regions overlap. More specifically, the checkpoints furthest downstream can share density information with checkpoints in their detection region. Therefore, in this implementation, checkpoints are only located at the element centres of the downstream boundaries. As illustrated in Figure 10, detection region lines are drawn towards these checkpoints, representing the detection region. Along each line, IPs are separated with length $l^{(\mathrm{IP;m})}$, which is chosen as the element size in

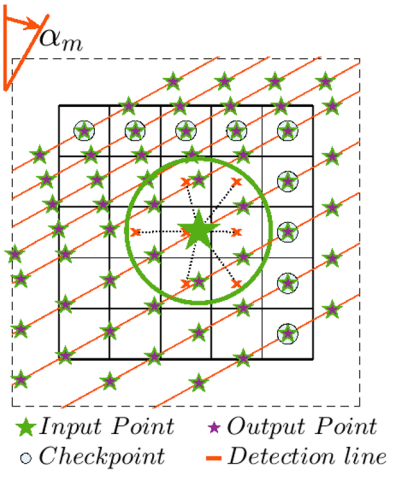

Figure 10. Schematic illustration of a milling access filter. For clarity, only one IP is highlighted. The checkpoints are at the downstream boundary elements. Milling orientation α_m determines the detection line orientation, and $\Omega^{(\mathrm{IP})}$ is marked by the dashed square.

x-direction $l^{(x)}$. The coordinates of the IPs can be calculated as follows:

$$\begin{aligned} \mathbf{c}_{k,i}^{(\mathrm{IP})} &= \mathcal{H}^{(\mathrm{m})}(\alpha) = \mathbf{c}_k - i\mathbf{r} \\ \text{with} \quad \mathbf{r} &= l^{(\mathrm{IP;m})} \begin{pmatrix} \cos(\alpha_m) \\ \sin(\alpha_m) \end{pmatrix} \\ \text{for} \quad i &= n_1, \ldots, n_2, \in \mathbb{Z}, \end{aligned} \tag{8}$$

where: $\mathbf{c}_k$ are the centre coordinates of the boundary element k; n_1 and n_2 are, respectively, the lowest and highest integer values of i resulting in an IP within the domain plus some spacing to account for $R^{(\mathrm{IP})}$, such that $\mathbf{c}_{k,i}^{(\mathrm{IP})} \in \boldsymbol{\Omega}^{(\mathrm{IP})}$.

A linear operation that ensures elements further downstream do not have a lower density than elements upstream is the cumulative sum:

$$\begin{aligned} \chi_{k,i}^{(\mathrm{OP})} &= \mathcal{F}^{(\mathrm{m})}\left(\chi^{(\mathrm{IP})}\right) \\ &= \begin{cases} \chi_{k,i}^{(\mathrm{IP})} & \text{for } i = n_1, \\ \chi_{k,i-1}^{(\mathrm{OP})} + \chi_{k,i}^{(\mathrm{IP})} & \text{for } n_1 < i \leq n_2, \end{cases} \end{aligned} \tag{9}$$

in which i is an integer index that runs along the IPs of a detection region line, and $\chi_i^{(\mathrm{IP})}$ and $\chi_i^{(\mathrm{OP})}$ are the input density and output density, respectively.

The OPs for the milling filter concide with IPs, and the values obtained from Equation (9) are projected from the OPs to the element centroids within $R^{(\mathrm{OP})}$.

The full milling filter procedure is summarized by the flowchart presented in Figure 11, visualizing how the output field $\bar{\mathbf{x}}$ is related to the input field $\tilde{\mathbf{x}}$ and the filter configuration design variable α_m. Observe that in Figure 11 a change in α smoothly influences the IP location. The IP location in turn influences $\chi^{(\mathrm{IP})}$, which influences the summation value $\chi^{(\mathrm{OP})}$ and ultimately the output field. Thus, sensitivities of the output field with respect to α can be calculated.

When multiple milling orientations are used in the manufacturing of the design, milling access from any considered milling orientation is sufficient for manufacturability. The combination of all milling access fields, for each orientation denoted here by ${}^{m}\bar{\mathbf{x}}$, yields $\bar{\mathbf{x}}^{(\min)}$. This can be achieved in

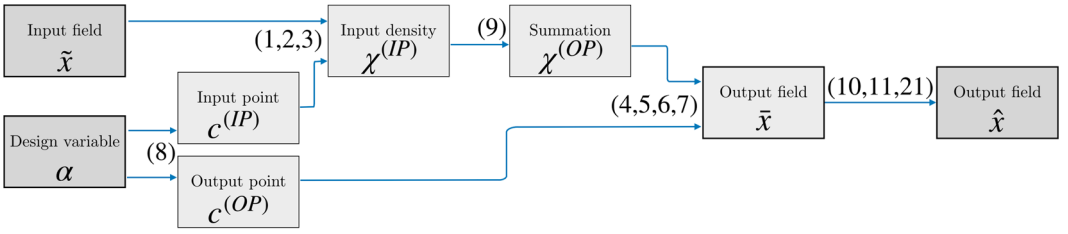

Figure 11. Schematic representation of how the output field $\hat{\mathbf{x}}$ is calculated, for the milling filter for one milling orientation. The numbers in parentheses represent the equations used for each step. By following the steps in reverse order, and through the chain rule, the sensitivities follow naturally.

a differentiable manner by applying the P-norm smooth minimum operator over the access fields of the different milling orientations:

$$\bar{x}_e^{(\min)} = \mathcal{G}_1^{(\mathrm{m})}(\bar{x}) = \left(\sum_{m=1}^{N^{(\mathrm{m})}} ({}^{m}\bar{x}_e)^{P_1} \right)^{1/P_1}. \tag{10}$$

Here, $P_1 < 0$ is the aggregation parameter, and $N^{(\mathrm{m})}$ is the number of milling orientations considered.

Note that the access field can have values higher than one, in fact in the order of the maximum number of elements in all directions. This has to be converted back to a density field with values ranging between zero and one. A P-norm smooth minimum function is used, involving the total access field and the maximum density value of one as

$$\bar{x}_e^{(\mathrm{out})} = \mathcal{G}_2^{(\mathrm{m})}\left(\bar{x}^{(\min)}\right) = \left(1 + \left(\bar{x}_e^{(\min)}\right)^{P_2}\right)^{1/P_2}. \tag{11}$$

Again, $P_2 < 0$ is the aggregation parameter.

3.2. Jetting with jet position optimization

This section presents a second example of application of the proposed framework, for the formulation of a jetting filter. A jetting filter ensures that the entire component's surface can be cleaned with fluid jets, as considered by Giele, Ayas, and Langelaar (2024), but now with simultaneous optimization of the jet source locations. From the jet source locations, the fluid is sprayed following straight lines in any direction, and should have access to the entire component's surface. In this article, for simplicity it is assumed that the jet source is a point, and a direct access from the source to the surface irrespective of the incoming jet angle will suffice (*i.e.* no secondary spray is considered). Note that this is equivalent to a visibility filter—see, for example, Chen, Lu, and Wei (2016). In density-based TO, this implies that, along each jetting line, regions further downstream are not permitted to have a lower density than those encountered upstream. Jet source locations have traditionally been defined a priori (Giele, Ayas, and Langelaar 2024). In this work, filter configuration design variables $\alpha_j^{(x)}$ and $\alpha_j^{(\mathrm{y})}$ are introduced that represent the $x-$ and $y-$coordinates of the jet source positions. Since the jetting filter has various similarities to the milling filter, for most of the filtering steps the reader is referred to Section 3.1, and only differences are described here. Similar to the milling section, in this section only one jet source is considered, and internal holes are not allowed.

In jetting, the detection regions are between the jet source location and each checkpoint, as visualized in Figure 12. Just as in milling, for computational reasons, only jet lines towards the (downstream)

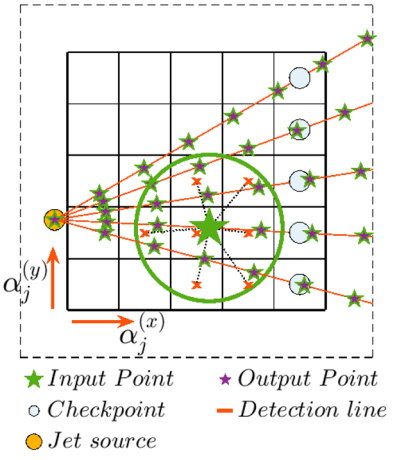

Figure 12. Jetting filter checkpoints and detection regions. For clarity, lines are only drawn on one domain boundary, and only one IP is highlighted. The checkpoints are at the downstream boundary elements. Jetting location α_j determines the detection line orientation, and $\Omega^{(\mathrm{IP})}$ is marked by the dashed square.

boundary element centres are used. The coordinates of each IP can be calculated as follows:

$$\begin{aligned} \mathbf{c}_{k,i}^{(\mathrm{IP})} &= \mathcal{H}^{(j)}(\alpha) = \boldsymbol{\alpha}_j + i\mathbf{r} \\ \text{with} \quad \mathbf{r} &= l^{(\mathrm{IP};j)} \begin{pmatrix} \cos(\beta_k) \\ \sin(\beta_k) \end{pmatrix} \\ \text{for} \quad i &= n_1, \ldots, n_2, \in \mathbb{Z}. \end{aligned} \tag{12}$$

Again, $l^{(\mathrm{IP};j)}$ is set to be the element size in the $x-$direction. β is the angle between the jet source location and the boundary element centre it is aiming at:

$$\beta_k = \cos^{-1}\left(\frac{c_k^{(x)} - \alpha_j^{(x)}}{c_k^{(y)} - \alpha_j^{(y)}} \right). \tag{13}$$

Again, $\mathbf{c}_k$ are the centre coordinates of the boundary element k; n_1 and n_2 are, respectively, the lowest and highest non-negative integer values of i resulting in an IP within the domain plus some spacing to account for $R^{(\mathrm{IP})}$, such that $\mathbf{c}_{k,i}^{(\mathrm{IP})} \in \Omega^{(\mathrm{IP})}$. The rest of the jetting filter steps are identical to those of the milling filter.

3.3. Printing with print direction optimization

In this section, a third example is given, to illustrate how the proposed method can be applied as a printing filter, inspired by Langelaar (2016), but now with simultaneous optimization of the printing direction. A printing filter ensures that a component can be manufactured with additive manufacturing. This requires the design to be self-supporting or, in other words, each new layer of material deposited is supported by previously deposited material, within the material and process dependent permissible overhang angles. In density-based TO, this can be ensured by a rule that a region further in the printing direction cannot have a density higher than that below. The 3D printing orientation and baseplate configuration in TO are traditionally defined a priori. In the first part of this section, the fixed printing orientation assumption will be relaxed. An additional relaxation of the baseplate configuration (orientation and height) is only considered in the second part of this section. The new filter

configuration design variable is angle α_p, which represents the angle between the printing orientation and the y-axis. For clarity and simplicity, the focus is on the 2D setting, where a single orientation variable suffices.

The checkpoints are located at the centres of all elements in the design domain. The detection region for each checkpoint k with coordinates $\mathbf{c}_k$ is the region opposite to the print orientation forming an arc of twice the overhang angle θ with a radius $l^{(\mathrm{IP};p)}$. In this region, three IPs are located (nine in a 3D implementation), as shown in Figure 13, with a distance of $l^{(\mathrm{IP};p)} = 1.5l^{(x)}$ from the checkpoint. The IPs are defined as

$$\begin{aligned} \mathbf{c}_{k,i}^{(\mathrm{IP})} &= \mathcal{H}^{(p)}(\alpha) = \mathbf{c}_k + \mathbf{r}_i \\ \text{with} \quad \mathbf{r}_i &= l^{(\mathrm{IP};p)} \begin{pmatrix} \cos(\alpha_p + \gamma_i) \\ \sin(\alpha_p + \gamma_i) \end{pmatrix} \\ \text{for} \quad \boldsymbol{\gamma} &= [-\theta, 0, \theta]. \end{aligned} \tag{14}$$

For clarity, the filter operation is written in two directly related parts, $\mathcal{F}_1^{(p)}$ and $\mathcal{F}_2^{(p)}$. The first operation function that ensures printability is a smooth maximum operation between the three input densities:

$$\chi_k^{(\max)} = \mathcal{F}_1^{(p)}\left(\chi^{(\mathrm{IP})}\right) = \left(\sum_{i=1}^{N^{(p)}} (\chi_{k,i}^{(\mathrm{IP})})^{P_3}\right)^{1/Q}, \tag{15}$$

where, following Langelaar (2016), $P_3 > 0$ is the aggregation parameter, and $Q = P_3 + (\log(N^{(p)})/\log(0.5))$, where $N^{(p)}$ is the number of IPs used. The second operation is a smooth minimum between the $\chi_k^{(\max)}$ value and the density value of the checkpoint element. This value, $\chi^{(k)}$, can also be interpreted as another input density with small radius, such that $\chi^{(k)} = \tilde{x}_e$, where element e is the element at checkpoint k, such that $\mathbf{c}^{(\mathrm{IP})} = \mathbf{c}_k$. The minimum value is calculated as follows:

$$\begin{aligned} \chi_k^{(\min)} &= \mathcal{F}_2^{(\mathrm{p})}\left(\chi^{(k)}, \chi^{(\max)}\right) \\ &= \frac{1}{2} \cdot \left(\left(\chi^{(k)} + \chi_k^{(\max)}\right) - \sqrt{\left(\chi^{(k)} - \chi_k^{(\max)}\right)^2 + \epsilon} + \sqrt{\epsilon} \right), \end{aligned} \tag{16}$$

where ϵ is a parameter that controls the smoothness of the minimum function, and where, for $\epsilon \to 0$, an exact non-smooth minimum operator is obtained. When no baseplate is considered, the output density value is the minimum value, such that $\chi_k^{(\mathrm{OP})} = \chi_k^{(\min)}$. The OP coincides with the checkpoint, and the output field is $\bar{\mathbf{x}}^{(\mathrm{out})}$ obtained with a small $R^{(\mathrm{OP})} < l^{(x)}$ such that $\chi^{(\mathrm{OP})}$ is projected to only one element.

In contrast to the previous filter examples, for the printing filter the operation function should be executed in a certain order. In previously proposed mesh-bound printing filters (*e.g.* Langelaar 2016), this results in a layer-by-layer operation. In the present filter with variable orientation, however, the order starts from the lowest unprocessed checkpoint in the printing orientation. The input density value $\chi^{(\mathrm{IP})}$ (from Equation 3) is thus calculated using the output values $\bar{\mathbf{x}}^{(\mathrm{out})}$. The authors note that these input values have always previously been calculated in a lower layer. Effectively, this sequential compound operation results in a filter function $\mathcal{F}$ that could complexly be written with only $\tilde{x}$ as input. The full procedure is summarized in Figure 14. Note in Figure 14 how a change in α influences the IP locations smoothly. This influences $\chi^{(\mathrm{IP})}$, which influences the maximum, $\chi^{(\max)}$, and minimum, $\chi^{(\min)}$, values. Ultimately the output field is influenced. Thus, sensitivities of the output field with respect to α can be calculated.

Also, note that, for this example filter, for simplicity the effect of changes in processing order due to changes in filter orientation variable is not accounted for in the sensitivity analysis. Neglecting this would probably not have a significant influence.

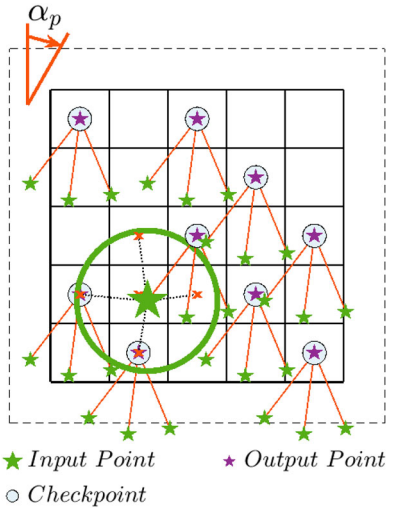

Figure 13. Schematic illustration of the printing filter, checkpoints and detection regions. For clarity, only a few checkpoints are drawn, and only one IP is highlighted. The distance between the checkpoint and the IP is $1.5l^{(x)}$ and is marked by the orange/grey lines.

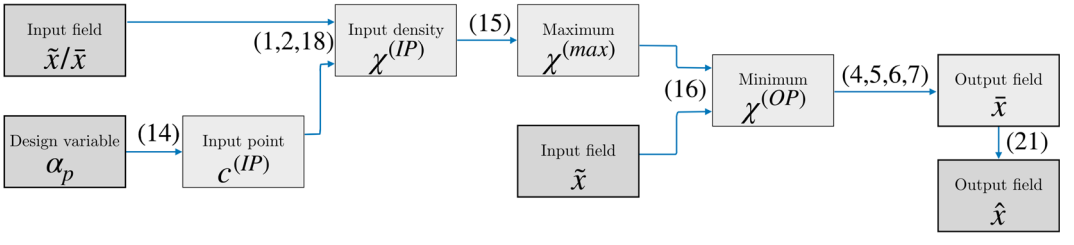

Figure 14. Schematic representation of the flow from the design variables to the output field, for the printing filter procedure without the baseplate consideration. The numbers in parentheses represent the equations used for each step. By following the steps backwards, and through the chain rule, the sensitivities follow naturally.

The second part of this section focuses on optimizing the baseplate height. Printing begins on the baseplate, meaning that only regions above the baseplate can be printed, whereas regions in the design domain below the baseplate cannot be printed. While this can be achieved in various ways, for the purpose of illustrating the versatility of the framework, a similar approach will be used here with output points. This differs from the previous examples in the sense that the density input gathering step is not required, and the framework is used to project a solid region into the domain. The baseplate height is defined by filter configuration design variable α_b. Recall that the orientation of the baseplate is linked to the print orientation α_p.

First, a field is created with the same discretization as the density field, $\mathbf{x}^{(\mathrm{BP})}$, with values of zero above the baseplate and values of one below the baseplate, including a smooth transition region around the baseplate with radius $R^{(\mathrm{OP;BP})}$. The transition region is required for gradient-based TO. In line with the framework, this field is created with OPs, whose location is based on α_p and α_b. One line of OPs, $R^{(\mathrm{OP;BP})}/2$ above the baseplate, project a value of $\chi^{(\mathrm{OP})} = 0$, while another line of OPs, $R^{(\mathrm{OP;BP})}/2$ below the baseplate, project a value of $\chi^{(\mathrm{OP})} = 1$, as shown in Figure 15. In this article, a radius $R^{(\mathrm{OP;BP})} = 3l^{(x)}$ is used, and the distance between neighbouring OPs on each line is $0.5l^{(x)}$.

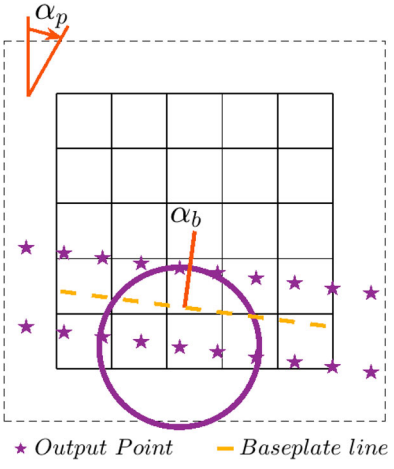

Figure 15. Printing baseplate field creation with OPs. For clarity of the figure, only one projection domain and $R^{(\mathrm{OP;BP})}$ is highlighted. The top row of OPs projects a value of $\chi^{(\mathrm{OP})} = 0$, the bottom row of OPs projects a value of $\chi^{(\mathrm{OP})} = 1$.

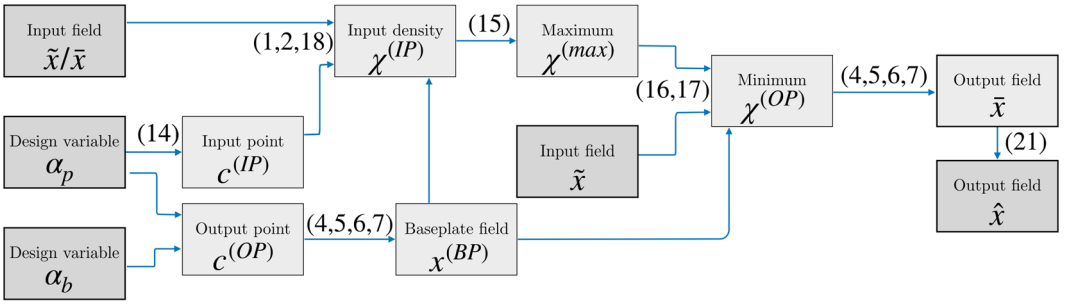

Figure 16. Schematic representation of the flow from the design variables to the output field, for the printing filter procedure including the baseplate consideration. The numbers in parentheses represent the equations used for each step. By following the steps backwards, and through the chain rule, the sensitivities follow naturally.

Elements in the baseplate field below the baseplate without OP contributions are given a value of $x_e^{(\mathrm{BP})} = 1$, which still leads to consistent sensitivities since only the transition region has an influence on the sensitivities of α_b and α_p.

The baseplate field $\mathbf{x}^{(\mathrm{BP})}$ can be used to create a printable output field only above the baseplate, such that for checkpoint k the output density is calculated:

$$\chi_k^{(\mathrm{OP})} = \mathcal{F}_3^{(p)}\left(\chi_k^{(\min)}, x_k^{(\mathrm{BP})}\right) = \chi_k^{(\min)}(1 - x_k^{(\mathrm{BP})}). \tag{17}$$

Also, it should be simulated that it is possible to print on the baseplate. This is done by adding $\tilde{x}_e$ and $x_e^{(\mathrm{BP})}$ in the detection region in Equation (3), such that this becomes

$$\chi^{(\mathrm{IP})}\left(\tilde{\mathbf{x}}, \mathbf{c}^{(\mathrm{IP})}, \mathbf{x}^{(\mathrm{BP})}\right) = \sum (\tilde{x}_e + x_e^{(\mathrm{BP})}) \check{w}_e^{(\mathrm{IP})}. \tag{18}$$

The procedure with baseplate consideration is shown in Figure 16.

4. Numerical examples

In this section, the numerical examples are presented and results are shown. Section 4.1 presents the problem formulation, including two extra steps to improve convergence and stability of the optimization, and the parameters used. Two-dimensional mechanical optimization problems on structured and unstructured meshes are presented in Section 4.2 and 4.3, respectively. Two 3D examples are presented in Section 4.4.

4.1. Problem formulation

For the numerical examples a mechanical optimization problem is considered with minimum compliance objective and a volume constraint. The density design variables are the input design field $\mathbf{x}$, which turn into the smoothed design $\tilde{\mathbf{x}}$, and the final geometric filtered design field is denoted by $\hat{\mathbf{x}}$.

The optimization problem is thus as follows:

$$\begin{aligned} \underset{\mathbf{x}}{\text{minimize}}: \quad & C(\hat{\mathbf{x}}) = \mathbf{u}^{\mathrm{T}}\mathbf{K}(\hat{\mathbf{x}})\mathbf{u} \\ \text{subjectto}: \quad & \mathbf{K}(\hat{\mathbf{x}})\mathbf{u} - \mathbf{f} = \mathbf{0} \\ & \frac{V(\hat{\mathbf{x}})}{V^*} - 1 \leq 0 \\ & 0 \leq x_e \leq 1 \quad \text{for } e = 1, \ldots, N_{\text{el}}. \end{aligned} \tag{19}$$

Here, $\mathbf{K}$, $\mathbf{u}$ and $\mathbf{f}$ denote the finite element system stiffness matrix, displacement vector and mechanical load vector, respectively. C is the compliance, the current design volume is V, the maximum allowed volume is V^*, and the number of elements in the domain is N_{el}.

In milling and jetting filters, the smoothed input design is turned into the filtered design by adding material downstream. Printing filters turn some input solid regions into void upon filtering, to remove unprintable features from the design. For the former, as explained by Giele, Ayas, and Langelaar (2024), numerical stability can be improved when volume evaluations are performed on the filtered design $\hat{x}$, while the unfiltered smoothed design $\tilde{x}$ is used for the finite element analysis.

Thus, for the milling and jetting filter, the optimization problem is modified as follows:

$$\begin{aligned} \underset{\mathbf{x}}{\text{minimize}}: \quad & C(\tilde{\mathbf{x}}) = \mathbf{u}^{\mathrm{T}}\mathbf{K}(\tilde{\mathbf{x}})\mathbf{u} \\ \text{subjectto}: \quad & \mathbf{K}(\tilde{\mathbf{x}})\mathbf{u} - \mathbf{f} = \mathbf{0} \\ & \frac{V(\hat{\mathbf{x}})}{V^*} - 1 \leq 0 \\ & 0 \leq x_e \leq 1 \quad \text{for } e = 1, \ldots, N_{\text{el}}. \end{aligned} \tag{20}$$

The proposed geometrical filters described in Section 2 sometimes put significant restrictions on the design, causing undesirable convergence behaviour. In this approach, the convergence is improved by gradually activating the geometric filters, similarly to the approach of van de Ven, Maas, *et al.* (2018). This is done by mixing the smoothed input design $\tilde{x}$ and the geometric filtered design $\bar{x}^{(\text{out})}$ with a general post filter function $\mathcal{G}^{(\text{g})}$:

$$\hat{x}_e = \mathcal{G}(\tilde{x}, \bar{x}^{(\text{out})}) = (1 - \eta)\tilde{x}_e + \eta\bar{x}_e^{(\text{out})}, \tag{21}$$

where $\eta \in [0, 1]$ is the scaling parameter. In this article, η is linearly increased from zero to one in the first 25 optimization iterations.

For the Young's modulus mapping in each element e in Equations (19) and (20), the modified Solid Isotropic Material with Penalisation (SIMP) interpolation scheme proposed by Sigmund (2007)

Table 1. Summary of the parameter values used in the numerical examples.

	All		Milling		Jetting		Printing	
Parameter	2D	3D	2D	3D	2D	3D	2D	3D
Filter radius, R	$1.5\,l^{(x)}$							
SIMP exponent, p	3.0							
$E_{\min}$	10^{-9}							
$E_{\max}$	1							
Poisson's ratio, ν	0.3							
Number of iterations	250							
IP distance, $l^{(\mathrm{IP})}$			$1.0\,l^{(x)}$	$1.0\,l^{(x)}$	$1.0\,l^{(x)}$	$1.0\,l^{(x)}$	$1.5\,l^{(x)}$	$1.9\,l^{(x)}$
IP radius, $R^{(\mathrm{IP})}$			$1.5\,l^{(x)}$	$1.75\,l^{(x)}$	$1.5\,l^{(x)}$	$1.75\,l^{(x)}$	$1.1\,l^{(x)}$	$1.25\,l^{(x)}$
OP radius, $R^{(\mathrm{OP})}$			$1.5\,l^{(x)}$	$1.75\,l^{(x)}$	$1.5\,l^{(x)}$	$1.75\,l^{(x)}$	$0.5\,l^{(x)}$	$0.5\,l^{(x)}$
OP radius, $R^{(\mathrm{OP;BP})}$							$4.5\,l^{(x)}$	$4.5\,l^{(x)}$
P_1			-2		-2			
P_2			-4		-4			
P_3							20	
ϵ							10^{-4}	
Overhang, θ							45°	
MMA move limits, α			0.2 rad		0.2	0.1	for α_p: 0.2 rad for α_b: 0.03	

is used, *i.e.*

$$E(\hat{x}_e) = E_{\min} + \hat{x}_e^p (E_{\max} - E_{\min}), \tag{22}$$

with penalization exponent $p = 3.0$, minimum and maximum Young's moduli $E_{\min} = 10^{-9}$ and $E_{\max} = 1$. For the finite element analysis, 4-node quadrilateral elements with bilinear shape functions are used for the 2D structured mesh, 3-node triangular elements with linear shape functions are used for the 2D unstructured mesh, and 8-node hexahedral elements with trilinear shape functions are used in 3D.

The 2D problem is implemented as an extension to the 88 line MATLAB® code by Andreassen *et al.* (2011), supplemented with the Method of Moving Asymptotes (MMA) optimizer by Svanberg (1987) with standard MMA parameter values. The 3D problem is implemented as an extension to the Portable and Extendable Toolkit for Scientific Computing (PETSc) code of Aage, Andreassen, and Lazarov (2015). The optimization is terminated after 250 iterations, by which number a desired level of convergence is always reached. The density filter radius is 1.5 element lengths, $1.5\,l^{(x)}$. An overview of the parameter values is given in Table 1. Using more IPs would lead to a better discretized approximation of the detection region, but would also increase computational costs. Bigger radii would lead to smoother optimization, but also include more information from outside the detection region. Consequently, these values are fixed, and their influence is not studied in this work.

For the new filter configuration design variables, it is important to mention the scaling (see also Figure 17) and MMA values used. In this implementation, $\alpha_m = 0$ implies vertical milling in the direction of the positive y-axis, and $\alpha_m = \pi/2$ implies horizontal milling in the direction of the positive x-axis. In this jetting filter implementation, the position variables $\alpha_j^{(x)}$ and $\alpha_j^{(y)}$ are normalized with the domain dimensions to range between zero and one. In this implementation, $\alpha_p = 0$ implies a vertical printing direction (in the positive y-direction), and $\alpha_p = \pi/2$ implies a horizontal printing direction (in the positive x-direction). In addition, for the base plate position, α_b is defined with respect to the domain centre, with $\alpha_b = 0$ impling the bottom of the domain, and $\alpha_b = 1$ the top. The filter configuration variables can have high sensitivities compared to the density variables, hence move limits are applied. The move limit used for the milling angle α_m is 0.2 rad (or approximately 11°), for the jetting location α_j it is 0.2, for the printing orientation α_p it is 0.2 rad (or approximately 11°), and for the printing baseplate height α_b it is 0.03.

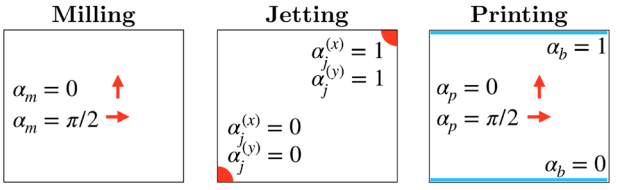

Figure 17. A schematic illustration of the scaled filter configuration design variables.

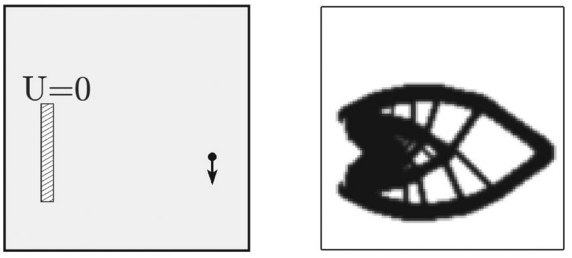

Figure 18. The 2D cantilever beam compliance problem. In (a), the load and boundary conditions are shown. The point load is applied 5% from the right edge, and 40% from the bottom. The fully clamped region is located 10% from the left edge, 40% from the bottom, and has a width of 2% and a height of 30%. In (b), the optimization result without geometry filters is shown. (a) Problem definition and (b) Reference design; $C := C_{\text{ref}}$.

4.2. 2D structured mesh

The first numerical example considers a 2D cantilever beam problem. This is a problem with well-known optimization behaviour. The boundary conditions and loading can be seen in Figure 18(a). A volume constraint of $V^* = 0.25$ is used, and the design domain is discretized by 100×100 elements. For comparison, the result of the standard optimization without the geometric filters is shown in Figure 18(b).

Next, the tests are done including the geometric filters. Two milling directions, three jet positions, or one printing orientation are considered. The initial filter configuration design variable values are given in Table 2, and given in the related figures. First, the example filters are applied without optimization of the filter configuration design variables. The resulting designs are shown in Figure 19. As can be seen, the designs obey the geometric constraints. Since the designs are highly restricted by the filters with fixed filter configuration design variables, the objective values are increased considerably, respectively by factors 1.420, 1.467 and 1.225 compared to the reference design in Figure 18. A comparison with existing methods that do not allow for optimization of filter configuration design variables is done in Appendix 2.

Next, the example filters are applied including optimization of the filter configuration design variables. The initial values for the filter configuration design variables are set to be their fixed values from the previous numerical example. The optimized designs can be seen in Figure 20, and the resulting filter configuration design variable values are reported in Table 2. As can be seen, the filter configuration design variable values have changed favourably. The relative objective values have improved with respect to the fixed filter variable example, specifically 1.381, 1.318 and 1.074 compared to the reference design. In the milling case, one milling orientation now has adjusted access to the left side of the component. It probably could lead to a better performance if the milling orientation would have rotated further, but apparently a local optimum was reached. In the jetting case, one jet moved to the left of the structure, allowing for a hole here and thus allocating the material more efficiently. In the printing case, allowing changes in printing orientation and baseplate height allowed a significantly

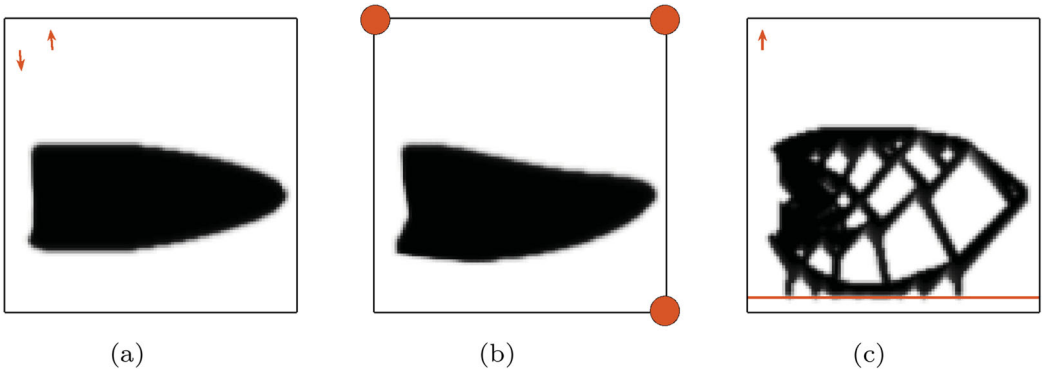

Figure 19. Results of the 2D cantilever beam compliance problem with fixed filter configuration design variables, obtained with (a) milling filter, (b) jetting filter, and (c) printing filter, with C_{ref} taken from Figure 18(b). (a) Milling filter; $C = 1.420C_{\text{ref}}$. (b) Jetting filter; $C = 1.467C_{\text{ref}}$ and (c) Printing filter; $C = 1.225C_{\text{ref}}$.

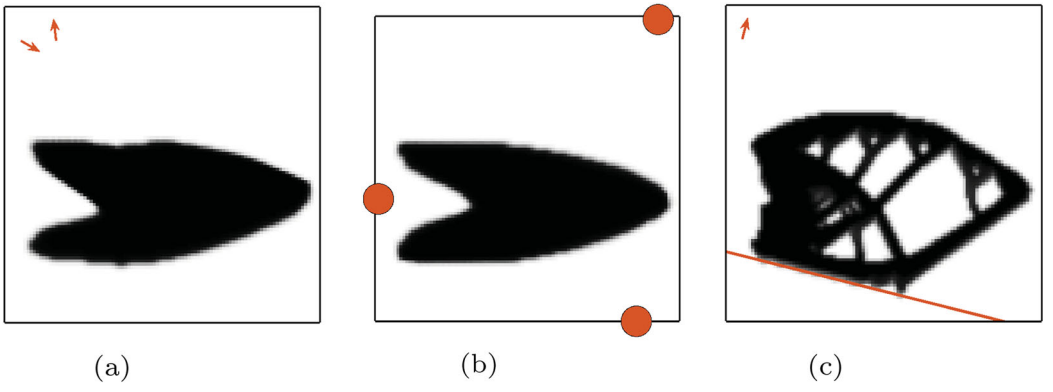

Figure 20. Results of the 2D cantilever beam compliance problem with optimized filter configuration design variables, obtained with (a) milling filter, (b) jetting filter, and (c) printing filter, with C_{ref} taken from Figure 18(b). (a) Milling; $C = 1.381C_{\text{ref}}$. (b) Jetting; $C = 1.318C_{\text{ref}}$ and (c) Printing; $C = 1.074C_{\text{ref}}$.

Table 2. Summary of filter configuration design variable values for 2D tests.

Filter	Variable	Fixed	Optimized	Unstructured
Milling	α_1	[0.09 ; −1.00]	[0.87 ; −0.50]	[−0.07 ; −1.00]
	α_2	[−0.09 ; 1.00]	[−0.10 ; 0.99]	[0.49 ; 0.87]
Jetting	α_1	[0.00 ; 1.00]	[0.01 ; 0.40]	[0.02 ; 0.38]
	α_2	[1.00 ; 1.00]	[0.93 ; 0.99]	[0.98 ; 0.98]
	α_3	[1.00 ; 0.00]	[0.86 ; 0.00]	[0.62 ; 0.00]
Printing	α_p	[0.00 ; 1.00]	[0.24 ; 0.97]	[0.31 ; 0.95]
	α_b	[0.05]	[0.11]	[0.10]

Notes: For clarity, the orientation design variables for milling and printing ($\boldsymbol{\alpha}_m$ and $\boldsymbol{\alpha}_p$) are described in vector notation, even though these are optimized as angles. The jetting design variables ($\boldsymbol{\alpha}_j$) are described in coordinates.

improved objective value. However, the nature of this filter, *e.g.* with elements close to the baseplate having a vast influence on the design, makes the optimization prone to local optima.

4.3. 2D unstructured mesh

Recall that an additional advantage of the proposed method is that it decouples the geometric filters from the mesh. Therefore, the method can readily be applied to optimization with an unstructured mesh.

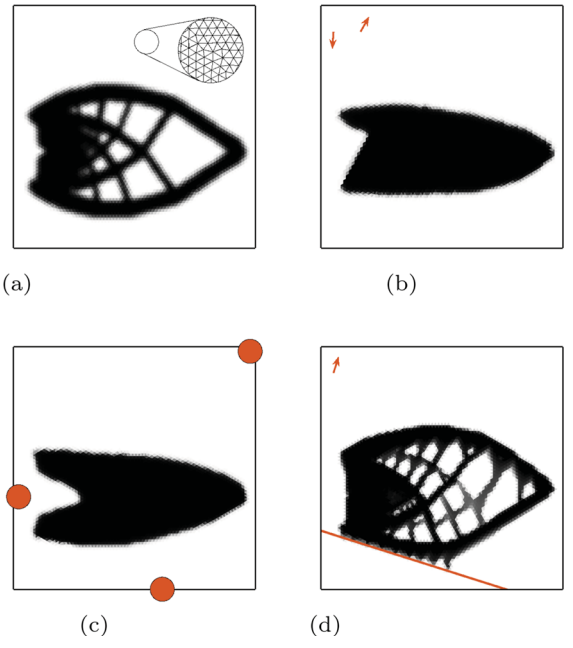

Figure 21. The results of the 2D cantilever beam compliance problem with optimized filter configuration design variables on an unstructured mesh, obtained with (a) no geometric filter, (b) milling filter, (c) jetting filter, and (d) printing filter. (a) Reference design, and close-up of the mesh; $C := C^{\Delta}_{\text{ref}}$. (b) Milling. $C = 1.507C^{\Delta}_{\text{ref}}$. (c) Jetting; $C = 1.393C^{\Delta}_{\text{ref}}$ and (d) Printing; $C = 1.134C^{\Delta}_{\text{ref}}$.

For the presented geometric filters, the most important difference between an unstructured and a structured mesh is that the element size is not constant. In this application, this is taken into account by assigning a weight to every element, $w_e^{(\text{area})}$, which is calculated with the element size normalized with respect to the average element size. This weight is subsequently included in Equation (1) as follows (and similarly in Equation 4):

$$w_e^{(\text{IP})} = \max(0, R^{(\text{IP})} - \|\mathbf{c}_e - \mathbf{c}^{(\text{IP})}\|) w_e^{(\text{area})}. \tag{23}$$

A mesh with triangular elements is created, with approximately 13,000 elements. The results for the method on an unstructured mesh are shown in Figure 21, and the improved filter configuration design variables are reported in Table 2. As can be seen, the results are similar to those reported in Figure 20, in geometric layout, optimized filter configuration design variable values, and objective values. This demonstrates versatility of the proposed method being suitable for an unstructured mesh. The grey elements in the printing case might be caused by the choice for the smooth maximum and minimum operations, but these regions might require further research.

4.4. 3D numerical examples

Next, the method is applied to two 3D problems discretized with a structured mesh. The first problem is a 3D cantilever beam problem with predictable optimization behaviour. The boundary conditions and applied loading can be seen in Figure 22(a). A volume constraint of $V^* = 0.10$ is used, and a discretization of $144 \times 192 \times 96$ elements is considered. For comparison, the result of the standard optimization without geometric filters is shown in Figure 22(b).

Again, the example filters are first applied with fixed filter configuration design variables. Two milling directions, four jet sources, and one printing orientation are considered. The initial values are shown on the left in Table 3, and in Figure 22.

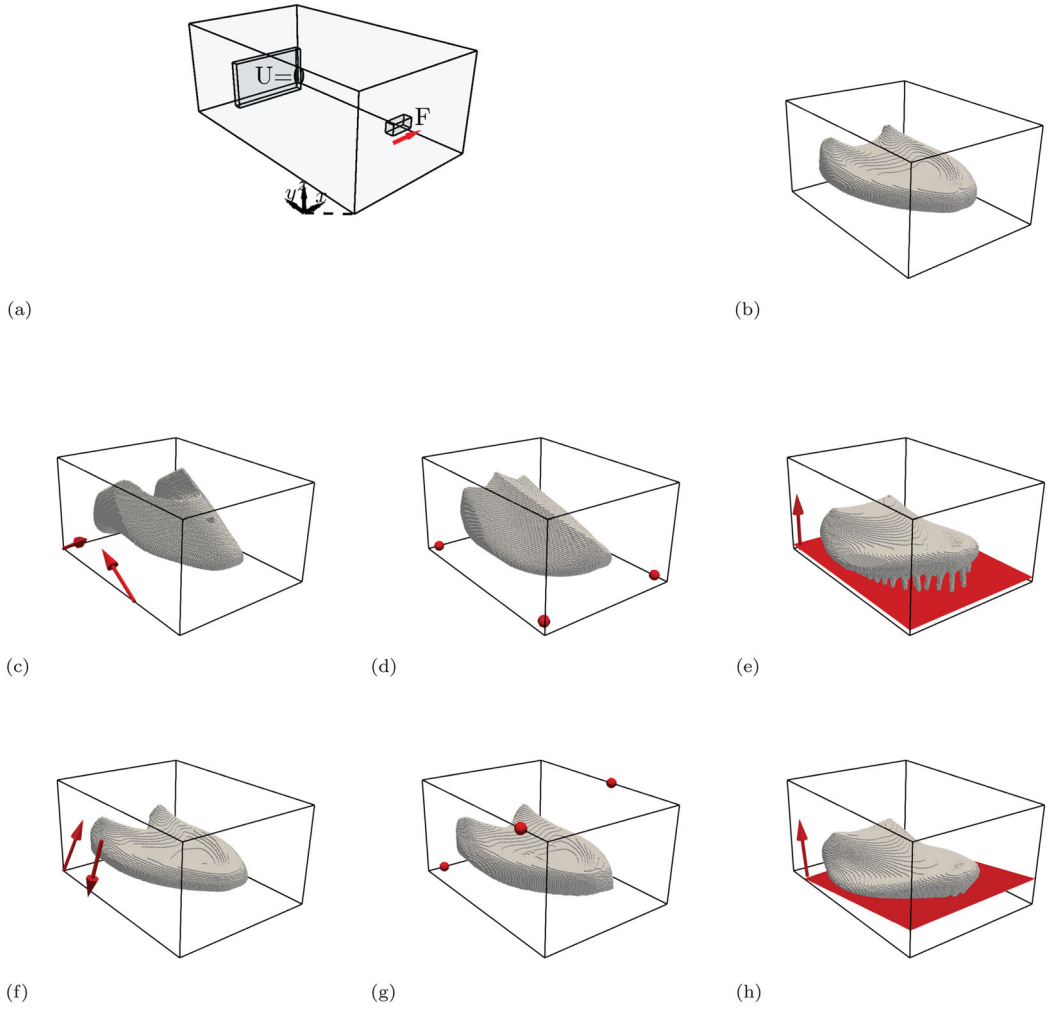

Figure 22. The 3D cantilever beam compliance problem definition and optimization results, with the geometric filters with both fixed and optimized filter configuration design variables, projected with a 0.5 density threshold value. (a) Load and boundary conditions. The problem has dimensions $L_x = 1.5$, $L_y = 2$ and $L_z = 1$. The load is applied in x-direction at $x \in [0.73, 0.77]$, $y \in [0.19, 0.21]$ and $z \in [0.39, 0.41]$. The fully clamped part is located at $x \in [0.375, 1.125]$, $y \in [1, 80, 1.90]$ and $z \in [0.2, 0.6]$. (b) Reference design without geometry filter; $C := C_{\text{ref}}$. (c) Result with milling filter, with fixed α; $C = 1.686C_{\text{ref}}$. (d) Result with jetting filter, with fixed α; $C = 1.385C_{\text{ref}}$. (e) Result with printing filter, with fixed α; $C = 1.258C_{\text{ref}}$. (f) Result with milling filter, with optimized α; $C = 1.146C_{\text{ref}}$. (g) Result with jetting filter, with optimized α; $C = 1.171C_{\text{ref}}$ and (h) Result with printing filter, with optimized α; $C = 1.272C_{\text{ref}}$.

Table 3. Summary of filter configuration design variable values for tests.

		Beam problem		Bridge problem	
Filter	Variable	Fixed	Optimized	Fixed	Optimized
Milling	α_1	[0 ; 0.87 ; 0.5]	[0.33 ; 0.20 ; 0.92]	[1; 0 ; 0]	[0.84 ; 0.00 ; −0.55]
	α_2	[0 ; −0.87 ; 0.5]	[−1.66 ; −0.20 ; −0.97]	[−1 ; 0 ; 0]	[−0.91 ; 0.40 ; −0.08]
Jetting	α_1	[0.075 ; 0.10 ; 0.05]	[1.88 ; 1.01 ; 0.00]	[1.40 ; −0.30 ; 0.53]	[1.50 ; 0.42 ; 0.42]
	α_2	[0.075 ; 0.90 ; 0.05]	[2.25 ; 1.71 ; 1.50]	[1.40 ; 1.30 ; 0.53]	[0.97 ; 2.42 ; 1.56]
	α_3	[0.925 ; 0.10 ; 0.05]	[0.00 ; 2.49 ; 1.50]	[−0.40 ; 3.30 ; 0.53]	[0.24 ; 2.10 ; 1.56]
	α_4	[0.925 ; 0.90 ; 0.05]	[0.28 ; 0.00 ; 0.00]	[−0.40 ; −0.30 ; 0.53]	[−0.50 ; 0.43 ; 0.42]
Printing	α_p	[0 ; 0 ; 1]	[−0.01 ; −0.14 ; 0.99]	[0 ; 0 ; 1]	[0 ; 0 ; 1]
	α_b	[0.05]	[0.13]	[0.02]	[0.03]

Notes: Again, for clarity, the orientation design variables for milling and printing ($\boldsymbol{\alpha}_m$ and $\boldsymbol{\alpha}_p$) are described in vector notation, even though these are optimized as angles. The jetting design variables ($\boldsymbol{\alpha}_j$) are described in coordinates.

The resulting designs can be seen in Figures 22(c)–22(e). As expected, the design freedom is severely restricted by the filters when using fixed filter configuration design variables. The relative objective values increased, by factors 1.686, 1.385 and 1.258, respectively. It would take numerous attempts for a designer to find the best filter configurations for these cases manually.

Next, the example filters are applied with optimization of the filter configuration design variables. The initial values for the filter configuration design variables are the respective fixed values depicted in Figures 22(c)–22(e). The results can be seen in Figures 22(f)–22(h). It is observed that the filter configuration design variables have changed significantly, and the resulting layouts are more similar to the unrestricted design shown in Figure 22(b). For the milling and jetting filters, the relative objective values have improved significantly by allowing the filter configuration design variables to change, to 1.146 and 1.171, respectively. For the printing filter, just as for the 2D examples, the baseplate has a significant impact on the entire design, and the new relative objective value is 1.272, slightly higher than the fixed filter configuration counterpart. For orientation optimization in combination with overhang constraints/filters, it is known that this problem can be very non-convex and multimodal in the orientation variables—see, for example, Langelaar (2018) and Olsen and Kim (2020). Small changes in baseplate orientation and height, just like small changes in material close to the baseplate, can have a big impact on the remaining design.

The second 3D problem is the bridge problem, for which the loading and boundary conditions are shown in Figure 23(a). To ensure that the geometric filters are effective near the top of the domain, a local low volume constraint is applied to a thin region, as previously done by Giele, van Keulen, and Langelaar (2022). A volume constraint of $V^* = 0.25$ of the unconstrained design domain is used, and a discretization of $64 \times 192 \times 72$ elements. For comparison, the result of the standard optimization without geometric filters is shown in Figure 23(b).

Two milling directions, four jet sources and one printing orientation are considered, and the jet sources are allowed outside the design domain. Again, first the example filters are applied with fixed filter configuration design variables. The initial values for the filter configuration design variables are shown in Table 3, and in Figure 23. The optimized designs are shown in Figures 23(c)–23(e). The initial filter variables are chosen such that, even when they are fixed, they are not too restrictive. However the objective values are still increased, by factors 1.190, 1.522 and 1.316, respectively. In Figures 23(f)–23(h), the results can be seen for the three example filters with optimization of the filter configuration design variables. The initial values for the filter configuration design variables are the respective fixed values depicted in Figures 23(c)–23(e). The relative objective values have changed to 1.311, 1.307 and 1.363, respectively.

In these 3D tests, the importance of the initial filter settings is noticeable. For both the milling and printing filters, the compliance is increased for the result with the optimized α. Since the initial filter settings are chosen to be more favourable, less improvement in the performance is obtained. The large influence of initialization, and the nonlinearity of the problem, probably result in a local minimum with a worse performance.

5. Discussion

The proposed method was found to be effective and adaptable for different geometric requirements. Still, several limitations are present with potential improvements.

First, the optimization of the filter configuration design variables may converge to an unfavourable local optima and is influenced by the initial filter setting values and several other parameters. Examples of this are to be seen in the results shown in Figure 20, where local optima are reached. In the experience of the present researchers, the most influential parameters are the initial filter configuration values, the MMA move limits and the scaling parameter η. Big changes in the filter configuration design variables throughout the optimization are unlikely as they are related to the current topology. In particular, the nature of the printing filter, where material right above the baseplate can alter the output design significantly, makes this problem prone to the local minima problem.

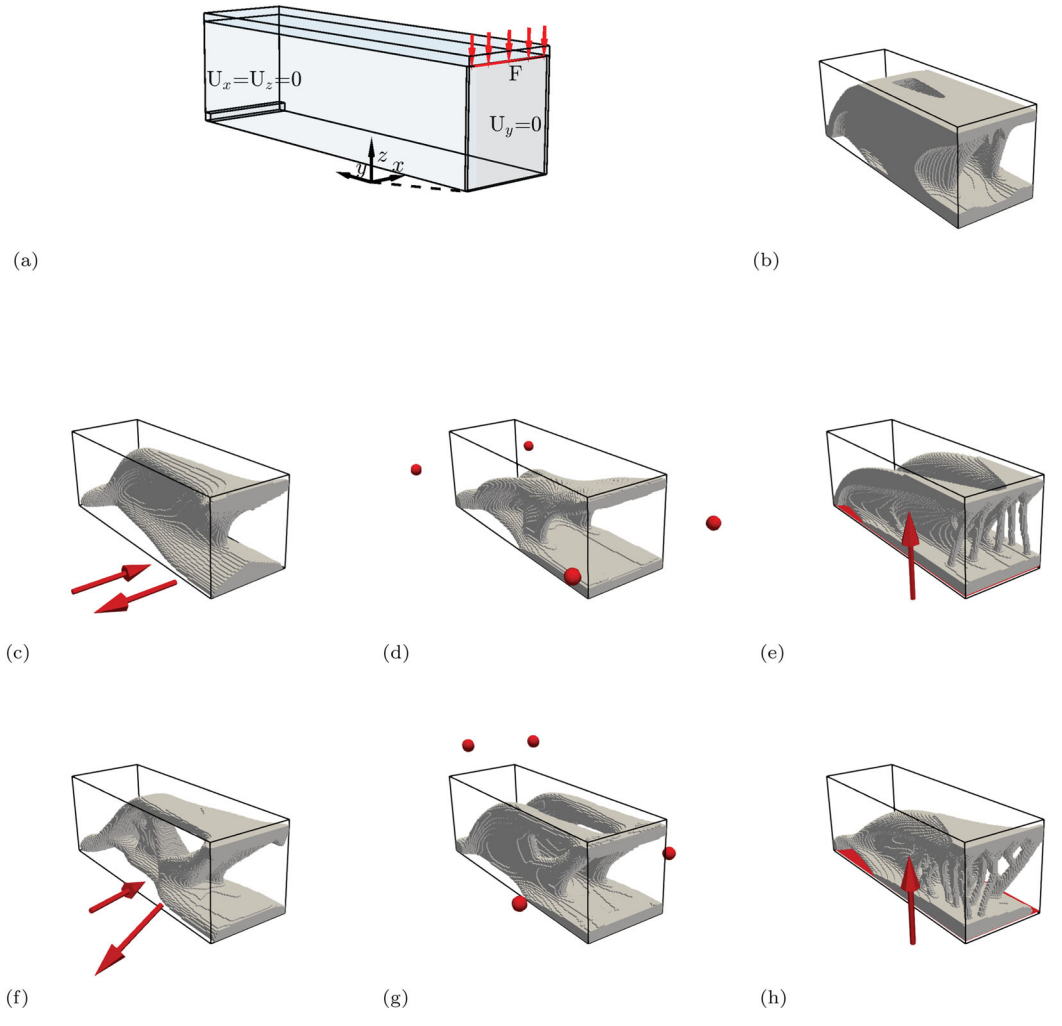

Figure 23. The 3D bridge compliance problem definition and optimization results, with the geometric filters with fixed filter configuration design variables, projected with a 0.5 density threshold value. (a) Boundary conditions for the 3D bridge problem. The problem has dimensions $L_x = 1$, $L_y = 3$ and $L_z = 1.0625$, where the top 0.0625 is involved in the local volume constraint. There is a symmetry boundary condition in the $x = 0$ plane, with a line load on top. The simply supported part is located at $x \in [0, 1]$, $y \in [2.98, 3.0]$ and $z \in [0, 0.02]$. (b) Reference design without geometry filter; $C := C_{\text{ref}}$. (c) Result with milling filter, with fixed α; $C = 1.190C_{\text{ref}}$. (d) Result with jetting filter, with fixed α; $C = 1.522C_{\text{ref}}$. (e) Result with printing filter, with fixed α; $C = 1.316C_{\text{ref}}$. (f) Result with milling filter, with optimized α; $C = 1.311C_{\text{ref}}$. (g) Result with jetting filter, with optimized α; $C = 1.307C_{\text{ref}}$. and (h) Result with printing filter, with optimized α; $C = 1.363C_{\text{ref}}$.

Secondly, for well chosen initial filter configurations, the improvement can be limited, see Figure 23. In this case, the filter adds unnecessary complexity to the optimization, which in some cases even resulted in (slightly) worse objective values.

Thirdly, the general concept of projecting densities to a mesh in a mesh-independent manner may also be of use in other operations, such as moving components through a mesh in feature-mapping TO methods, which offers opportunities for future research.

Next, the influence of $R^{(\text{IP})}$ is discussed: a bigger radius allows for more information on the detection region, resulting in a less crisp detection region and a smoother convergence, but also more intermediate density values and increasing computational costs. A minimum possible radius of one element length is recommended, and higher values when convergence characteristics require this.

Similarly, the influence of the finite number of checkpoints and input points should be discussed. The number of checkpoints is generally kept the same as the number of finite elements, since the influence of a higher level of refinement is negligible. The number of input points should be such that a good sampling of the detection region is obtained. A higher number would increase computational cost, whereas an insufficient number could lead to discretization dependency or failure to meet the geometric requirements.

Lastly, performance comparisons should be made to existing case-specific methods that allow for optimization of the filter configuration design variables, specifically those of Olsen and Kim (2020), Wang and Qian (2020), Wang (2022) and Gasick and Qian (2021).

6. Conclusion

A general framework is presented applicable for any geometric filtering operations. In this novel scheme, the filter operation is decoupled from the mesh using interpolated densities. This allows for a continuous description of the filter configuration, and subsequently for introducing new filter configuration design variables that can be optimized simultaneously with the topology with consistent sensitivities leading to increased design freedom and performance. The specific scenarios where this framework adds new capabilities are cases where it is desired to optimize the filter configuration variables. Instead of defining custom filters for that purpose, this framework inherently enables this, in a unified manner. Examples are jetting with moving locations, printing with changing orientation, milling with changing tool orientation, casting with changing release direction and mold parting surface, *etc.*

As shown by the three numerical examples, the framework can be applied to various different geometric filters. The numerical examples showed that the initial filter configuration chosen has a strong influence on the design. Allowing this configuration to be optimized simultaneously with the topology, as enabled by the proposed method, can thus result in significantly improved designs with superior objective values. For examples with a well chosen initial filter configuration, the improvement in objective value is limited, and in some cases the method and additional design freedom may actually add complexity to the optimization, resulting in convergence to (slightly) inferior local optima.

The biggest challenge, and thus recommendation for future work, is therefore regarding the prevalence of local optima. Most noticeable in the printing example, but also in other examples, is that small changes in filter configuration may weaken the design significantly.

Finally, the article also introduces a general framework for how to approach geometric filters. Any geometry requirement can be enforced through wise consideration of the detection region. Any initial design decision can be optimized with extended design freedom. Through this philosophy, engineers are encouraged and enabled to develop novel adaptive filters for their specific use cases.

Acknowledgments

The authors wish to thank Krister Svanberg for providing the MATLAB MMA code.

Disclosure statement

No potential conflict of interest was reported by the author(s).

Funding

This publication is part of the project RECIPE [project number 17977 of the research programme HTSM], which is (partly) financed by the Dutch Research Council (NWO).

Data availability statement

The necessary information for replication of the results is present in the manuscript. To help readers reproduce results, further algorithm details or data will be provided upon reasonable request.

ORCID

Reinier Giele http://orcid.org/0009-0009-8218-3659

References

Aage, Niels, Erik Andreassen, and Boyan S. Lazarov. 2015. "Topology Optimization Using PETSc: An Easy-to-Use, Fully Parallel, Open Source Topology Optimization Framework." *Structural and Multidisciplinary Optimization* 51 (3): 565–572. https://doi.org/10.1007/s00158-014-1157-0.

Andreassen, Erik, Anders Clausen, Mattias Schevenels, Boyan S. Lazarov, and Ole Sigmund. 2011. "Efficient Topology Optimization in MATLAB Using 88 Lines of Code." *Structural and Multidisciplinary Optimization* 43 (1): 1–16. https://doi.org/10.1007/s00158-010-0594-7.

Bourdin, Blaise. 2001. "Filters in Topology Optimization." *International Journal for Numerical Methods in Engineering* 50 (9): 2143–2158. https://doi.org/10.1002/nme.116.

Bruns, Tyler E., and Daniel A. Tortorelli. 2001. "Topology Optimization of Non-linear Elastic Structures and Compliant Mechanisms." *Computer Methods in Applied Mechanics and Engineering* 190 (26-27): 3443–3459. https://doi.org/10.1016/S0045-7825(00)00278-4.

Chen, Yonghua, Jianan Lu, and Ying Wei. 2016. "Topology Optimization for Manufacturability Based on the Visibility Map." *Computer-Aided Design and Applications* 13 (1): 86–94. https://doi.org/10.1080/16864360.2015.1059199.

Delissen, Arnoud, Elwin Boots, Dick Laro, Harry Kleijnen, Fred van Keulen, and Matthijs Langelaar. 2022. "Realization and Assessment of Metal Additive Manufacturing and Topology Optimization for High-Precision Motion Systems." *Additive Manufacturing* 58:103012. https://doi.org/10.1016/j.addma.2022.103012.

Gasick, Joshua, and Xiaoping Qian. 2021. "Simultaneous Topology and Machine Orientation Optimization for Multiaxis Machining." *International Journal for Numerical Methods in Engineering*122 (24): 7504–7535. https://doi.org/10.1002/nme.6839.

Gaynor, Andrew T., and James K. Guest. 2016. "Topology Optimization considering Overhang Constraints: Eliminating Sacrificial Support Material in Additive Manufacturing through Design." *Structural and Multidisciplinary Optimization* 54 (5): 1157–1172. https://doi.org/10.1007/s00158-016-1551-x.

Gersborg, Allan Roulund, and Casper Schousboe Andreasen. 2011. "An Explicit Parameterization for Casting Constraints in Gradient Driven Topology Optimization." *Structural and Multidisciplinary Optimization* 44 (6): 875–881. https://doi.org/10.1007/s00158-011-0632-0.

Giele, Reinier, Can Ayas, and Matthijs Langelaar. 2024. "Fluid Jet Access in Topology Optimization for Cleanable Parts." *Computers and Structures* 301:107420. https://doi.org/10.1016/j.compstruc.2024.107420.

Giele, Reinier, Fred van Keulen, and Matthijs Langelaar. 2022. "Design for Drainability in Density-Based Topology Optimization." *Structural and Multidisciplinary Optimization* 65 (6): 1–14. https://doi.org/10.1007/s00158-022-03272-3.

Høghøj, Lukas Christian, and Erik A. Träff. 2022. "An Advection–Diffusion Based Filter for Machinable Designs in Topology Optimization." *Computer Methods in Applied Mechanics and Engineering* 391:114488. https://doi.org/10.1016/j.cma.2021.114488.

Langelaar, Matthijs. 2016. "Topology Optimization of 3D Self-supporting Structures for Additive Manufacturing." *Additive Manufacturing* 12:60–70. https://doi.org/10.1016/j.addma.2016.06.010.

Langelaar, Matthijs. 2017. "An Additive Manufacturing Filter for Topology Optimization of Print-Ready Designs." *Structural and Multidisciplinary Optimization* 55 (3): 871–883. https://doi.org/10.1007/s00158-016-1522-2.

Langelaar, Matthijs. 2018. "Combined Optimization of Part Topology, Support Structure Layout and Build Orientation for Additive Manufacturing." *Structural and Multidisciplinary Optimization* 57 (5): 1985–2004. https://doi.org/10.1007/s00158-017-1877-z.

Langelaar, Matthijs. 2019. "Topology Optimization for Multi-axis Machining." *Computer Methods in Applied Mechanics and Engineering* 351:226–252. https://doi.org/10.1016/j.cma.2019.03.037.

Mirzendehdel, Amir M., Morad Behandish, and Saigopal Nelaturi. 2020. "Topology Optimization with Accessibility Constraint for Multi-axis Machining." *CAD Computer Aided Design* 122:102825. https://doi.org/10.1016/j.cad.2020.102825.

Olsen, Jack, and Il Yong Kim. 2020. "Design for Additive Manufacturing: 3D Simultaneous Topology and Build Orientation Optimization." *Structural and Multidisciplinary Optimization* 62 (4): 1989–2009. https://doi.org/10.1007/s00158-020-02590-8.

Sigmund, Ole. 2007. "Morphology-Based Black and White Filters for Topology Optimization." *Structural and Multidisciplinary Optimization* 33 (4-5): 401–424. https://doi.org/10.1007/s00158-006-0087-x.

Svanberg, Krister. 1987. "The Method of Moving Asymptotes—A New Method for Structural Optimization." *International Journal for Numerical Methods in Engineering* 24 (2): 359–373. https://doi.org/10.1002/nme.1620240207.
van de Ven, Emiel, Can Ayas, Matthijs Langelaar, Robert Maas, and Fred van Keulen. 2018. "A PDE-Based Approach to Constrain the Minimum Overhang Angle in Topology Optimization for Additive Manufacturing." In *Proceedings of the World Congress of Structural and Multidisciplinary Optimisation (WCSMO 2017)*, 1185–1199. Cham, Switzerland: Springer. https://doi.org/10.1007/978-3-319-67988-4_89.
van de Ven, Emiel, Robert Maas, Can Ayas, Matthijs Langelaar, and Fred van Keulen. 2018. "Continuous Front Propagation-Based Overhang Control for Topology Optimization with Additive Manufacturing." *Structural and Multidisciplinary Optimization* 57 (5): 2075–2091. https://doi.org/10.1007/s00158-017-1880-4.
Wang, Cunfu. 2022. "Simultaneous Optimization of Build Orientation and Topology for Self-supported Enclosed Voids in Additive Manufacturing." *Computer Methods in Applied Mechanics and Engineering*388:114227. https://doi.org/10.1016/j.cma.2021.114227.
Wang, Cunfu, and Xiaoping Qian. 2020. "Simultaneous Optimization of Build Orientation and Topology for Additive Manufacturing." *Additive Manufacturing* 34:101246. https://doi.org/10.1016/j.addma.2020.101246.
Yoon, Gil Ho, and Seon Il Ha. 2021. "A New Development of a Shadow Density Filter for Manufacturing Constraint and Its Applications to Multiphysics Topology Optimization." *Journal of Mechanical Design, Transactions of the ASME* 143 (6): 1–20. https://doi.org/10.1115/1.4048818.

Appendices

Appendix 1. Sensitivity analysis

This section gives an example of how the sensitivities can be calculated for the optimization of the filter configuration design variables. All equations can be traced to Figures 11 and 16. By simply following the steps in reverse, and using the chain rule, the sensitivities with respect to $\tilde{x}$ and α can be calculated.

In the following, only one part is shown, *i.e.* the part described in Figure 6. If the sensitivities of compliance C (or any other response) with respect to an input density, $\chi_i^{(\mathrm{IP})}$, are called $\mathrm{d}C/\mathrm{d}\chi_i^{(\mathrm{IP})}$, the sensitivities for the density design variables can be calculated with the chain rule and Equation (3):

$$\frac{\mathrm{d}C}{\mathrm{d}\tilde{x}_e} = \sum_{i=1}^{N_{\mathrm{IP}}} \frac{\mathrm{d}C}{\mathrm{d}\chi_i^{(\mathrm{IP})}} \frac{\mathrm{d}\chi_i^{(\mathrm{IP})}}{\mathrm{d}\tilde{x}_e} \quad \text{with} \quad \frac{\mathrm{d}\chi_i^{(\mathrm{IP})}}{\mathrm{d}\tilde{x}_e} = \check{w}_{e,i}^{(\mathrm{IP})}. \tag{A1}$$

Here, N_{IP} refers to the total number of IPs. Similarly, to obtain the sensitivities with respect to the position of a single IP omitting the subscript i for clarity, first the sensitivities for $\check{w}_e^{(\mathrm{IP})}$ can be calculated with the chain rule and Equation (3):

$$\frac{\mathrm{d}C}{\mathrm{d}\check{w}_e^{(\mathrm{IP})}} = \frac{\mathrm{d}C}{\mathrm{d}\chi^{(\mathrm{IP})}} \frac{\mathrm{d}\chi^{(\mathrm{IP})}}{\mathrm{d}\check{w}_e^{(\mathrm{IP})}} \quad \text{with} \quad \frac{\mathrm{d}\chi^{(\mathrm{IP})}}{\mathrm{d}\check{w}_e^{(\mathrm{IP})}} = \tilde{x}_e. \tag{A2}$$

Next, the sensitivities for $w_e^{(\mathrm{IP})}$ can be calculated with the chain rule and Equation (2):

$$\frac{\mathrm{d}C}{\mathrm{d}w_e^{(\mathrm{IP})}} = \frac{\mathrm{d}C}{\mathrm{d}\check{w}_e^{(\mathrm{IP})}} \frac{\mathrm{d}\check{w}_e^{(\mathrm{IP})}}{\mathrm{d}w_e^{(\mathrm{IP})}} \quad \text{with} \quad \frac{\mathrm{d}\check{w}^{(\mathrm{IP})}}{\mathrm{d}w_e^{(\mathrm{IP})}} = \frac{1}{\sum_{j=1}^{N_{\mathrm{el}}} w_j^{(\mathrm{IP})}} + \frac{-w_e^{(\mathrm{IP})}}{\left(\sum_{j=1}^{N_{\mathrm{el}}} w_j^{(\mathrm{IP})}\right)^2}. \tag{A3}$$

Subsequently, the sensitivities for $\mathbf{c}^{(\mathrm{IP})}$ can be calculated with the chain rule and Equation (1):

$$\frac{\mathrm{d}C}{\mathrm{d}\mathbf{c}^{(\mathrm{IP})}} = \frac{\mathrm{d}C}{\mathrm{d}w_e^{(\mathrm{IP})}} \frac{\mathrm{d}w_e^{(\mathrm{IP})}}{\mathrm{d}\mathbf{c}^{(\mathrm{IP})}} \quad \text{with} \quad \frac{\mathrm{d}w^{(\mathrm{IP})}}{\mathrm{d}\mathbf{c}^{(\mathrm{IP})}} = \begin{cases} 0 & \text{if} \quad R^{(\mathrm{IP})} - \|\mathbf{c}_e - \mathbf{c}^{(\mathrm{IP})}\| < 0, \\ \dfrac{\mathbf{c}_e - \mathbf{c}^{(\mathrm{IP})}}{\|\mathbf{c}_e - \mathbf{c}^{(\mathrm{IP})}\|} & \text{otherwise.} \end{cases} \tag{A4}$$

For computational reasons, in cases of $\mathbf{c}_e = \mathbf{c}^{(\mathrm{IP})}$ it is possible to add a small offset preventing division by zero. Lastly, in a similar manner, the sensitivities for Equations (4)–(18) can be computed. Specifically the derivatives from operation $\mathcal{H}$—shown in Equations (8), (12) and (14)—will result in the sensitivities for α.

Appendix 2. Comparison with the existing methods

This section presents optimized designs using geometric filters from the literature. More specifically, the work of Langelaar (2019) was used for milling, that of Giele, Ayas, and Langelaar (2024) was used for jetting and that of Langelaar (2017) was used for printing. The results can be seen in Figure A1.

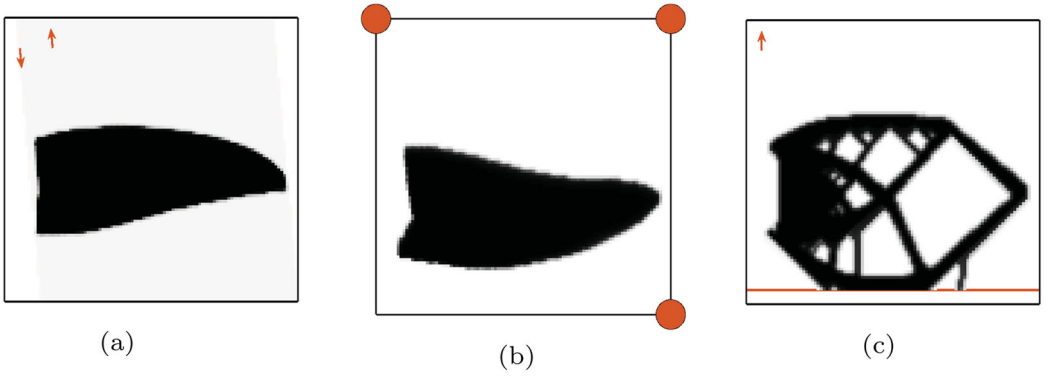

Figure A1. Results of the 2D cantilever beam compliance problem with the existing methods from the literature, which do not account for configuration design variables, obtained with (a) a milling filter (Langelaar 2019), (b) a jetting filter (Giele, Ayas, and Langelaar 2024) and (c) a printing filter (Langelaar 2017), with C_{ref} taken from Figure 18(b). (a) Milling filter; $C = 1.464C_{\mathrm{ref}}$. (b) Jetting filter; $C = 1.455C_{\mathrm{ref}}$ and (c) Printing filter; $C = 1.094C_{\mathrm{ref}}$.

Visually comparing Figures 19 and A1 shows that the proposed filters based on density interpolation give designs that are qualitatively similar to those obtained by existing methods. Quantitatively, the design performances are also similar, but differences are observed owing to convergence to different local optima. This is most apparent in the case of the overhang filter. The relative compliances obtained are as follows: $C = 1.464C_{\mathrm{ref}}$ for the milling method by Langelaar (2019) and $C = 1.420C_{\mathrm{ref}}$ for the proposed milling method; $C = 1.455C_{\mathrm{ref}}$ for the jetting method by Giele, Ayas, and Langelaar (2024) and $C = 1.467C_{\mathrm{ref}}$ for the proposed jetting method; $C = 1.094C_{\mathrm{ref}}$ for the printing method by Langelaar (2017) and $C = 1.225C_{\mathrm{ref}}$ for the proposed printing method.